Int. J. Electrochem. Sci., 17 **(2022)** Article Number: 221054, doi: 10.20964/2022.10.53

International Journal of
ELECTROCHEMICAL
SCIENCE
www.electrochemsci.org

Electrodeposited SnO_2/graphene composite as highly effective and stable anticorrosion coating for aluminum alloys in acidic environments

Jingqi Zhu, Jianming Han, Wenjun Yu, Nankun Geng, Yunxiao Wan, Yiting Peng[*], *Huaijie Cao*[*], *Qunjie Xu*[*]

Shanghai Key Laboratory of Materials Protection and Advanced Materials in Electric Power, Shanghai University of Electric Power, Shanghai, 200090, China.
[*]E-mail: pyt_1108@shiep.edu.cn, hjcao0510@shiep.edu.cn, xuqunjie@shiep.edu.cn

Received: 20 July 2022 / *Accepted:* 19 August 2022 / *Published:* 10 September 2022

Using cyclic voltammetry, a SnO_2/graphene (SnO_2/G) composite coating was electrodeposited on an aluminum alloy in this study. The morphology and composition of this coating were analyzed by scanning electron microscopy (SEM), X-ray diffraction (XRD) and X-ray photoelectron spectroscopy (XPS). Electrochemical impedance spectroscopy (EIS) measurements were performed to evaluate the stability and corrosion resistance of the coating. Moreover, the deposit formation mechanism and anticorrosion mechanism of the composite coating were investigated. The results showed that for electrodeposition conditions with a GO concentration of 0.06 mg/ml and a potential range of 0.6 ~ -1.1 V (vs. SCE) at a scanning rate of 25 mV/s, the composite coating showed good stability in a strong mixed acid solution (0.5 M H_2SO_4 + 2 ppm HF). The protection efficiency of the deposited coating, which was immersed in an acidic solution for more than 70 h on an aluminum alloy substrate, remained greater than 99.33%, indicating good long-term stability of the composite coating.

Keywords: SnO_2/graphene, electrodeposition, aluminum alloy, corrosion

1. INTRODUCTION

As promising materials, aluminum alloys have been applied in various fields, including the aerospace, automotive, shipping and chemical industries, because they are lightweight and strong and exhibit good plasticity and superior mechanical performance [1~3]. However, the poor corrosion resistance of aluminum alloys in specific environments limits their usage. Corrosion-resistant coatings containing polymer materials and inorganic nonmetallic materials have been widely used to protect metals such as copper, aluminum and stainless steel [4,5]. Metal oxide semiconductors, such as tin oxide (SnO_2), titanium dioxide (TiO_2), and zinc oxide (ZnO), are well known for their use in lithium-

ion battery materials and solar cell materials [6~9]. Among them, tin oxide (SnO_2), which is a wide-band gap n-type semiconductor, is an important and widely applied metal oxide semiconductor [10]. Due to its excellent chemical stability, high light transmittance and other advantages, it has attracted the attention of researchers. Researchers have prepared Ti/SnO_2 electrodes by depositing SnO_2 on titanium sheets to degrade organic contaminants in wastewaters by electrochemical oxidation. Furthermore, a SnO_2 coating deposited on the surface of an aluminum alloy by a hydrothermal method was shown to have good corrosion resistance [11]. Therefore, SnO_2 is a good choice for protecting metals from corrosion.

Additionally, graphene is an sp^2 hybridized carbon coating with a single atomic layer thickness. Researchers have extensively explored its properties for use in the fields of science and technology [12]. Due to its physical and chemical advantages, such as excellent electrical conductivity and good mechanical properties, it is widely used in supercapacitors [13~15], batteries [16], fuel cells [17], and solar energy units [18]. Furthermore, graphene has been reported for corrosion protection [19~22]. Jin et al. [23] used graphene-coated Cu micronanosheet building blocks to assemble bulk Gr/Cu composites that exhibited excellent corrosion resistance in simulated seawater.

Graphene and tin dioxide composite coatings exhibit excellent electrical conductivity. Researchers have applied SnO_2/G nanocomposites to lithium-ion battery electrode materials, sensors, capacitors and other fields [24~26]. However, few studies have been reported on the application of SnO_2/G composites in the field of metal protection via anticorrosive coatings.

Therefore, graphene can be combined with tin dioxide by electrodeposition to prepare a corrosion-resistant SnO_2/G composite coating, which can be applied to an aluminum alloy surface for corrosion protection. In our work, an efficient and easy-to-operate method was first presented to prepare highly anticorrosive nanocomposite coatings on aluminum alloys via electrodeposition. The aluminum alloy was anodized in an acid solution using a potentiostat, followed by cyclic voltammetry to electrodeposit the SnO_2/G composite coating on the substrate to strengthen aluminum anticorrosion resistance. Under mixed acid conditions of 0.5 M H_2SO_4 and 2 ppm HF, the as-prepared coating showed very high corrosion resistance and high inhibition efficiency. More importantly, after 72 h of immersion in the mixed acids, the substrate with the deposits maintained good corrosion resistance.

2. EXPERIMENTAL

2.1 Materials and chemicals

The material studied herein was aluminum alloy 5052 (40 mm × 13 mm × 2 mm, purchased from Jieguan Industrial Cleaning Water Treatment Technology Co., LTD, Hangzhou, China). The main elements of the alloy and the element contents are shown in Table 1. All chemical reagents were purchased from Aladdin Chemical Reagent Co., Ltd. and were of analytical grade. They were used as received without further purification.

Table 1. Main elements and their content in the aluminum alloy

Element	Si	Fe	Cu	Mn	Mg	Cr	Zn	Al
Content(wt.%)	0.25	0.4	0.1	0.1	2.5	0.15	0.1	96.4

2.2 Electrodeposition of the SnO_2/G nanocomposite coating

2.2.1. Aluminum alloy substrate pretreatment.

After the AA5052 alloy (50 mm × 10 mm × 2 mm) was polished, it was ultrasonically washed with acetone and ethanol. The aluminum alloy plate was connected to the positive electrode of the electrochemical station, and a platinum plate (20 mm × 20 mm × 2 mm) was connected to the negative electrode of a potentiostat. Then, a voltage of 20 V was applied between the two electrodes (4 cm apart), and the aluminum alloy was electrochemically polished in a perchloric acid alcohol solution ($V_{ethanol}$: $V_{perchloric\ acid}$ = 1:4) for 3 min (in an ice-water bath). The electrochemically polished aluminum alloy was anodized in a 0.2 M phosphoric acid solution for 30 min in a 50 °C water bath (voltage between the two electrodes was 30 V). The aluminum alloy processed by the above steps was sonicated in a 1 wt.% phytic acid solution for 10 min and then dried in a vacuum drying oven (35 °C, -0.1 MPa) for 8 h.

2.2.2 Preparation of the deposition solution.

Graphene oxide (GO) with a concentration of 0.06 mg/L, $SnCl_2 \cdot 2H_2O$, HNO_3, KNO_3, and pyrrolidone K-30 were dissolved in deionized water, and the mixed solution was prepared at a predetermined concentration and stirred well. The mixed solution was oxygenated for 1 h in a 50 °C water bath.

2.2.3. Preparation of the SnO_2/G composite coating by electrodeposition.

A three-electrode system was used for electrodeposition. The working electrode, counter electrode and reference electrode corresponded to the aluminum alloy, platinum electrode (20 mm × 20 mm × 2 mm) and saturated calomel electrode, respectively. Cyclic voltammetry (CV) was used for electrodeposition at a water bath temperature of 60 °C and a sweep rate of 25 mV/s.

2.3 Sample characterizations

X-ray diffraction (XRD) patterns were recorded using a Bruker D8 Advance X-ray diffractometer (Cu Kα, λ = 1.5406 Å) with a scan speed of 5°/min. The surface morphologies, microstructures and chemical compositions of the samples were investigated by using scanning electron microscopy (SEM, JSM-7800F, JEOL, Japan, operated at 5 kV), while the deposit

composition on the surface of the AA 5052 samples was analyzed by Fourier transform infrared spectrometry (FTIR-8400S, SHIMADZU, Japan) at a resolution of 4 cm^{-1} in a range of 4000-400 cm^{-1}, and Raman measurements were performed on a Lab RAM HR Evolution (λ=633 nm). Additionally, X-ray photoelectron spectroscopy (XPS, Thermo Scientific ESCALAB 250Xi) was conducted to analyze the compositions of the samples using a monochromatic Al Kα source with a pass energy of 25 eV.

Electrochemical properties were determined in a 0.5 M H_2SO_4 + 2 ppm HF aqueous solution at room temperature using an electrochemical workstation with a standard three-electrode system. The specific connection of each electrode was the same as above. The polarization curve was measured at a rate of 1 mV/s scan between -250 mV and 250 mV (vs. OCP). In addition, at a frequency in the range of 100,000 Hz to 0.01 Hz with an amplitude of 10 mV, electrochemical impedance spectroscopy (EIS) measurements were performed. Finally, to investigate the stability and long-term corrosion resistance of the composite coating, polarization was carried out for 6 h at 0.6 V (vs. SCE) and -0.1 V (vs. SCE), and the current density versus time curves were recorded.

3. RESULTS AND DISCUSSION

3.1 Cyclic voltammetry curve

Preparation of the SnO_2/G composite coating was performed via cyclic voltammetry, as shown in Figure 1. A cathode peak at -0.65 V (vs. SCE) and the corresponding current density of 40.38 mA cm^{-2} can be seen in Figure 1(a). This peak may be due to the reduction of NO_3^- ions or due to Sn^{2+} on the electrode surface, as shown in Equations (1) and (2). Sn^{4+} is obtained by oxidizing Sn^{2+} with oxygen in solution or by oxidizing Sn^{2+} with nitric acid. Sn^{4+} reacts with OH^- in the solution to form unstable $Sn(OH)_4$, and $Sn(OH)_4$ easily decomposes to form SnO_2, thereby forming a SnO_2 coating on the surface of the cathode, as shown in Equations (3) and (4) [27]. The oxidation peak that appeared during the negative scan is caused by the oxidation of Sn^{2+} to Sn^{4+}. As shown in Figure 1(b), the reduction peak continuously decreases with the increase in the number of scanning cycles, which is due to the continuous decrease in the concentration of NO_3^- ions.

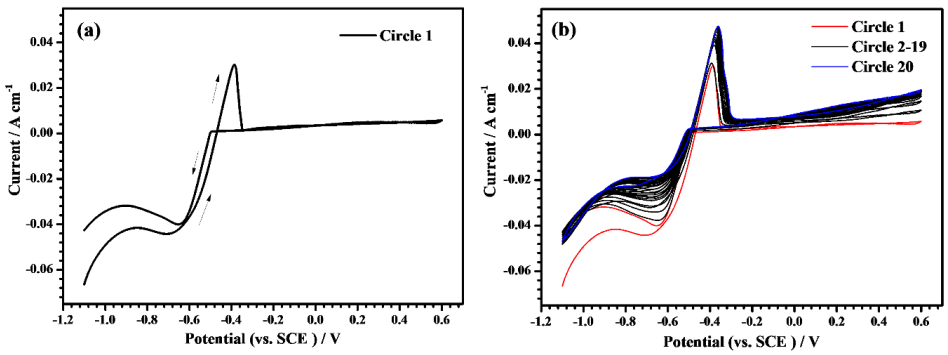

Figure 1. (a) CV curve of the first cycle of the SnO_2/G composite coating prepared by electrodeposition; (b) CV curve for 20 cycles of the SnO_2/G composite coating prepared by electrodeposition with a potential range from 0.6 to -1.1 V (vs. SCE) at 60 °C. The solution contained 0.06 mg/L GO, $SnCl_2 \cdot 2H_2O$, HNO_3, KNO_3, and pyrrolidone K-30.

$$NO_3^- + H_2O + 2e^- \rightarrow NO_2^- + 2OH^- \quad (1)$$

$$Sn^{2+} + O_2 + 2H_2O + 2e^- \rightarrow Sn^{4+} + 4OH^- \quad (2)$$

$$Sn^{4+} + 4OH^- \rightarrow Sn(OH)_4 \quad (3)$$

$$Sn(OH)_4 \rightarrow SnO_2 + 2H_2O \quad (4)$$

3.2 Morphology and chemical composition of the surface

SEM images of the SnO_2/G composite coating deposited on the aluminum alloy surface are provided in Figure 2. According to these images, the outermost layer of the deposit coating uniformly covers a graphene layer, and the graphene layer completely covers the entire surface and is tightly combined with the lower layer. Based on the notch in the graphene coating, the lower layer is composed of SnO_2 nanospheroidal particles with a diameter of 200-300 nm. The SnO_2 nanospheres exhibit a uniform particle size. Moreover, the distribution of the three elements (Figure 3) shows that they are almost evenly distributed over the entire surface, indicating that the outermost layer of the graphene coating is not composed of a single layer of graphene. It is a composite coating formed by graphene and SnO_2 particles, which have smaller particle sizes (1-10 nm). From Table 2, which shows the percentage of each element on the surface, the atomic percentage for surface C of the composite coating is 21.72%, the atomic percentage of O is 52.63%, and the atomic percentage of Sn is 25.33%, wherein C is mainly derived from graphene, and Sn and O come from SnO_2 (Sn:O≈2:1).

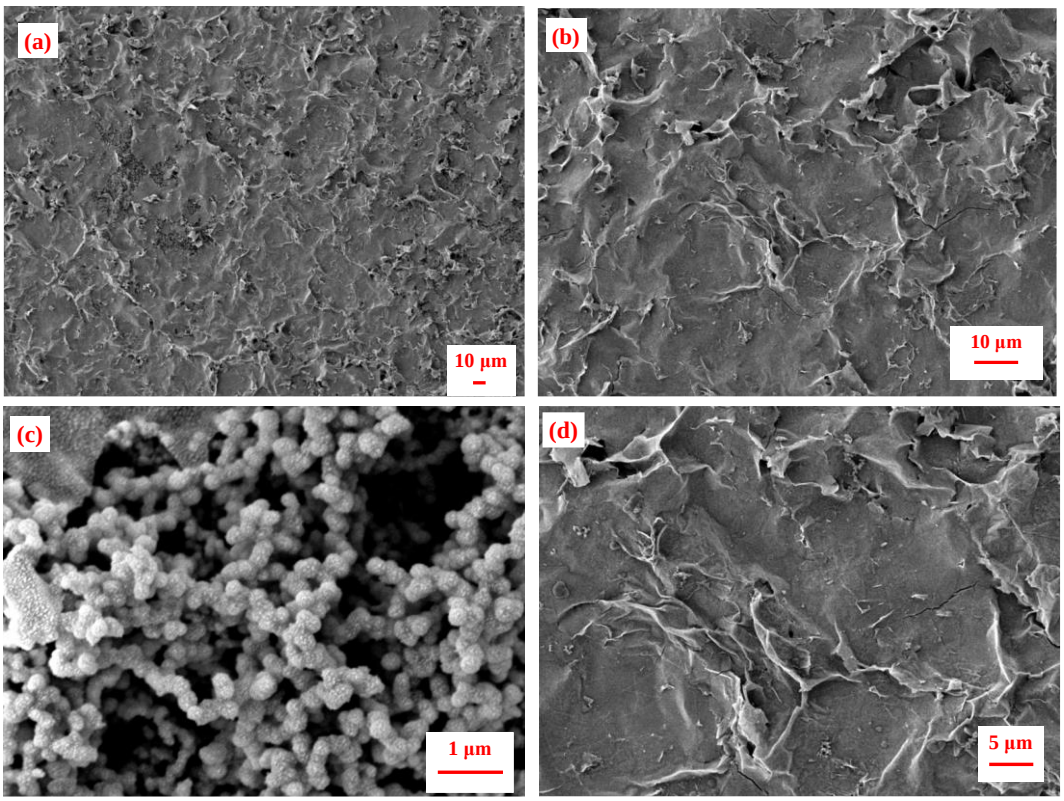

Figure 2. SEM images of the SnO_2/G composite coating prepared at 60 °C with a potential range from 0.6 to -1.1 V (vs. SCE).

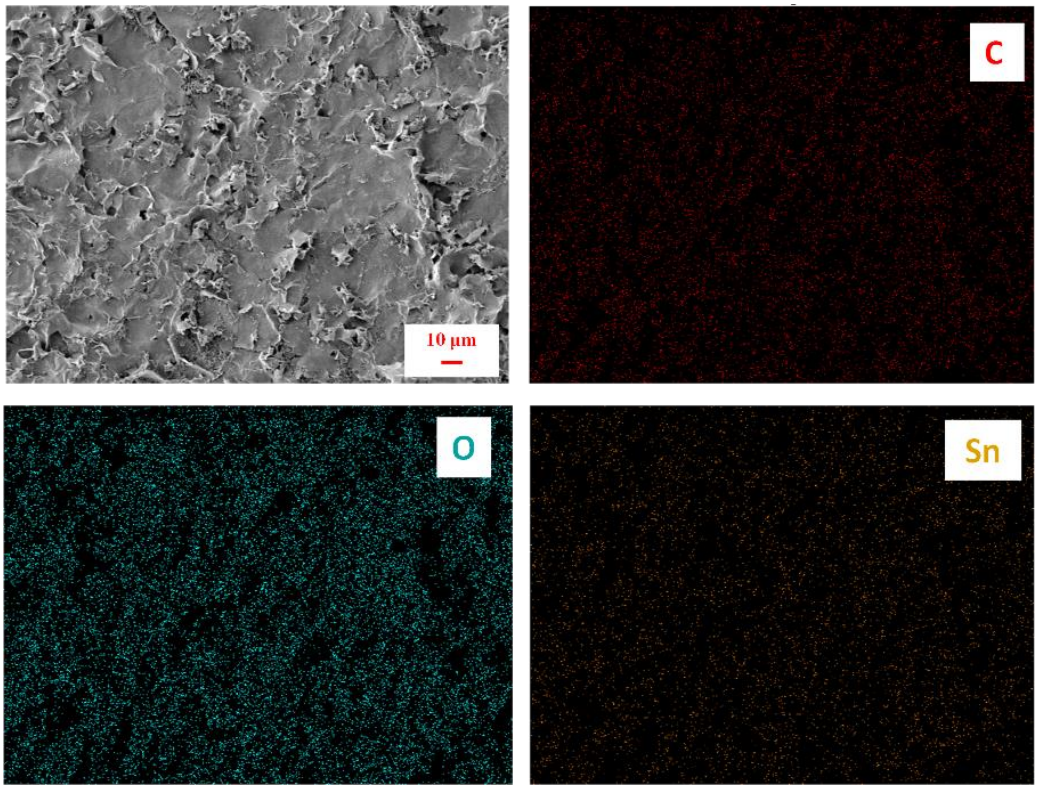

Figure 3. The distribution of the elements on the SnO_2/G composite coating prepared at 60 °C with a potential range from 0.6 to -1.1 V (vs. SCE).

Table 2. The elemental content of the SnO_2/G composite coating prepared at 60 °C with a potential range from 0.6 to -1.1 V (vs. SCE).

Element	Line type	Apparent concentration	k	Wt.%	Wt.% Sigma	Atomic percentage
C	K	24.51	0.24509	6.34	0.22	21.72
O	K	54.60	0.47838	20.45	0.61	52.63
Mg	K	0.14	0.00128	0.04	0.10	0.06
Al	K	0.66	0.00599	0.17	0.11	0.26
Sn	M	200.31	2.00310	73.01	0.79	25.33
Total amount:				100.00		100.00

To further analyze the thickness of the deposit on the alloy and the distribution of SnO_2 and graphene in the composite coating, SEM and mapping are used to study the cross section of the SnO_2/G coating. According to the SEM image in Figure 4, the SnO_2/G composite coating is very dense and tightly bonded to the aluminum alloy substrate. In addition, the composite coating and aluminum alloy substrate can be clearly distinguished in the mapping plot. The elemental distribution of the

section is the same as that of the surface. Moreover, the thickness of the SnO_2/G composite coating is approximately 100 μm, as shown in Figure 4.

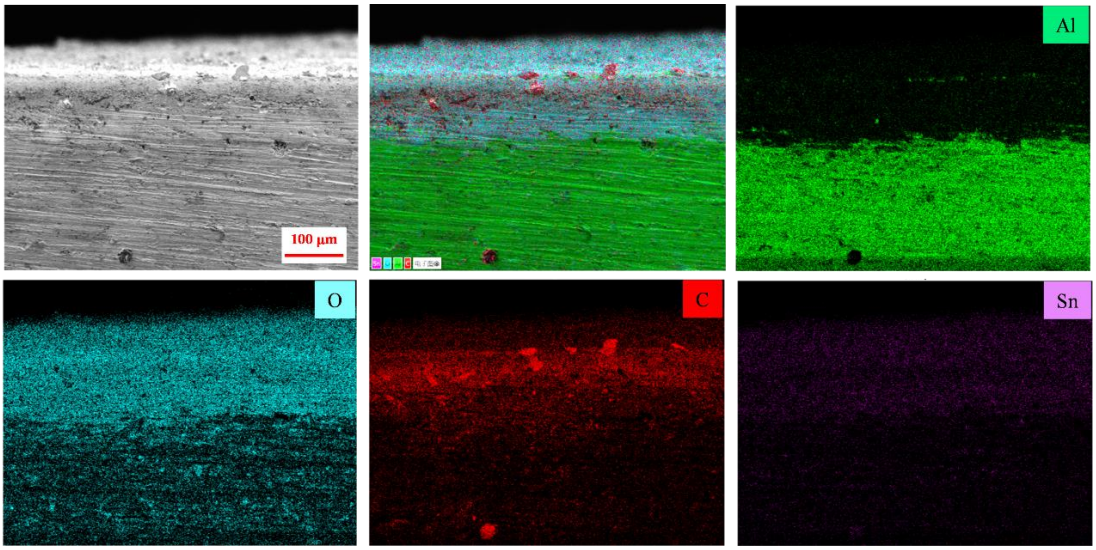

Figure 4. Cross-sectional SEM images and EDS mapping of the SnO_2/G composite coating prepared at 60 °C with a potential range from 0.6 to -1.1 V (vs. SCE).

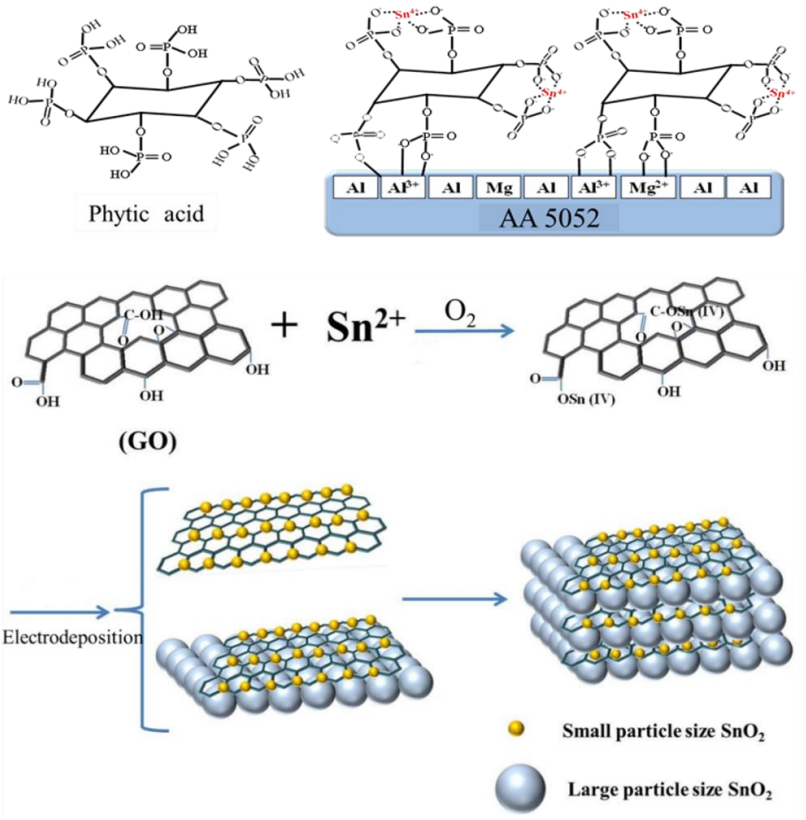

Figure 5. Schematic diagram of the SnO_2/G composite coating on the aluminum alloy surface

Therefore, by combining the surface SEM and the cross-sectional SEM with the elemental distribution diagram, the morphology of the SnO_2/G composite coating prepared by cyclic voltammetry on the surface of the aluminum alloy can be clearly seen, as shown in Figure 5. Specifically, Figure 5 illustrates that there are two types of SnO_2 in the prepared composite layer. The SnO_2 nanospheres have a particle diameter of 200-300 nm, and the SnO_2 particles have very small particle diameters and are embedded in the graphene defects.

The X-ray diffraction (XRD) patterns of GO and the SnO_2/G composite coating are shown in Figure 6. The diffraction peak at 2θ=9.5 in the XRD pattern of the GO sample is a characteristic peak for GO, which indicates that the weak van der Waals forces between the graphite layer and the layer are destroyed under the action of the oxygen-containing functional groups, thereby forming graphene oxide composed of a monolayer or a few flaked layers. The peaks in the XRD pattern of the composite coating are an exact match to the standard card (PDF# 41-1445) of the tetragonal rutile structure of SnO_2. The diffraction peak for GO does not appear, indicating that graphene is present instead of oxidized graphite [28,29].

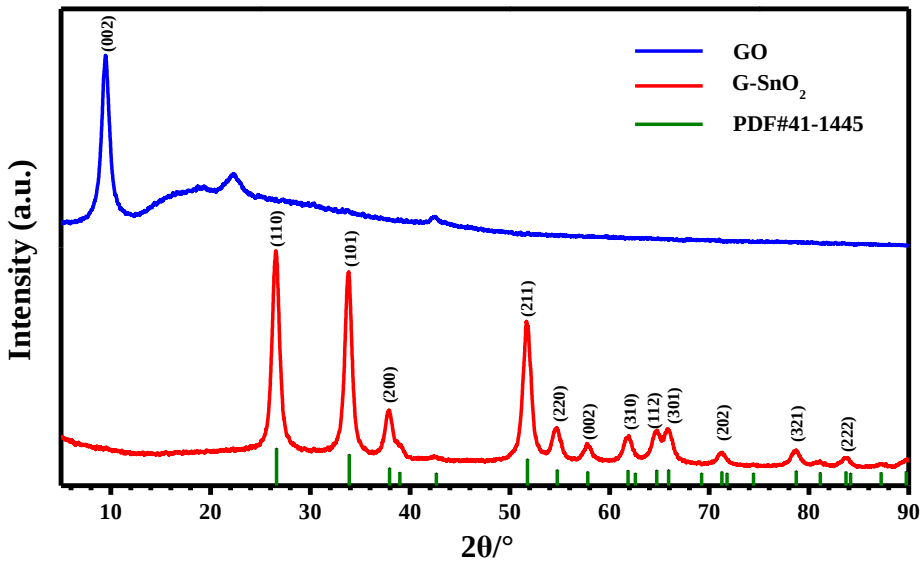

Figure 6. XRD pattern of GO and the SnO_2/G composite coating prepared at 60 °C with a potential range from 0.6 to -1.1 V (vs. SCE).

As an effective characterization tool, XPS is mainly used for analyzing the chemical composition and chemical valence of materials on the surface. Figure 7 illustrates the XPS spectra of the SnO_2/G composite coating and GO. As shown in Fig. 7 (a), in the SnO_2/G composite coating XPS spectrum, the SnO_2/G composite coating contains C, Sn, O, N, Cl, and P, wherein N comes from the surfactant pyrrolidone K-30 and HNO_3, Cl is derived from $SnCl_2$, and P is derived from phytic acid (before electrodeposition, the surface of the aluminum alloy is treated with phytic acid). As shown in Fig. 7(b), the Sn 3d XPS spectrum of the SnO_2/G composite coating has two strong peaks at 495.3 eV and 486.9 eV, corresponding to Sn $3d_{3/2}$ and Sn $3d_{5/2}$, respectively, which suggests that Sn was successfully deposited in the form of SnO_2 on the surface of the aluminum alloy after electrodeposition [30]. Combined with Fig. 7(c), the C 1s XPS spectra of GO can be divided into peaks at 284.6, 285.1,

286.2 and 288.4 eV, which correspond to C-C/C=C (sp^2 C), C-OH, C-O-C (epoxy groups) and C=O, respectively. The C 1s XPS spectrum of the SnO_2/G composite coating only gave two peaks for C-C/C=C (284.6 eV) and C-OH (286.2 eV) after peak separation. By comparing the C 1s XPS spectra of GO and SnO_2/G, it is found that there are no C-O-C (epoxy group) and C=O peaks in the C 1s XPS spectrum of SnO_2/G, and the relative peak intensity of C-OH is noticeably small. This clearly shows that GO is reduced to graphene (G) during electrodeposition.

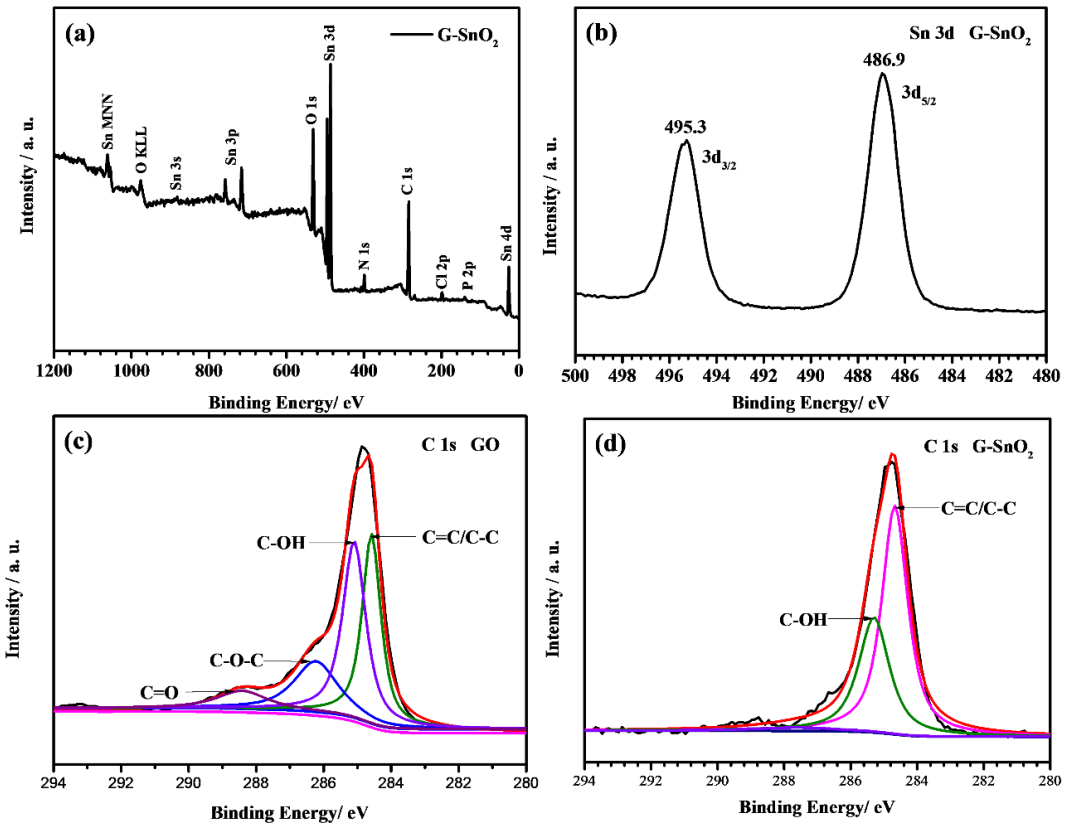

Figure 7. XPS spectra of the SnO_2/G composite coating prepared at 60 °C with a potential range from 0.6 to -1.1 V (vs. SCE): (a) XPS survey scan of SnO_2/G, (b) Sn 3d XPS spectra of SnO_2/G, (c) C 1s XPS spectrum of GO, and (d) C 1s XPS spectrum of SnO_2/G

To further explore the structure of carbon-based materials, Raman spectroscopy was used for analysis. After the electrodeposition process, the Raman spectrum of the carbon material changes significantly (as shown in Figure 8). From this figure, the Raman spectra of the GO and SnO_2/G composite coatings show D and G peaks at 1340.6 nm and 1610.9 nm, respectively. The G peak represents the sp^2 C vibration in graphene (E_{2g} phonon vibration), and the D peak represents the vibration of sp^3 C in graphene (the κ-point phonon vibration of A_{lg}), which is related to the destruction of the hexagonal and symmetric lattice structure of graphene. Generally, the intensity ratio of I_D to I_G (I_D/I_G) values is used to characterize the degree of defects in graphene [31~32]. Therefore, the I_D/I_G values of the GO and SnO_2/G composite coatings according to the spectrum are 1.06 and 1.86, respectively, which illustrate that the average size of the sp^2 region on the SnO_2/G composite coating prepared by GO electrodeposition was smaller, and the smaller SnO_2 nanoparticles were successfully embedded in GO [33].

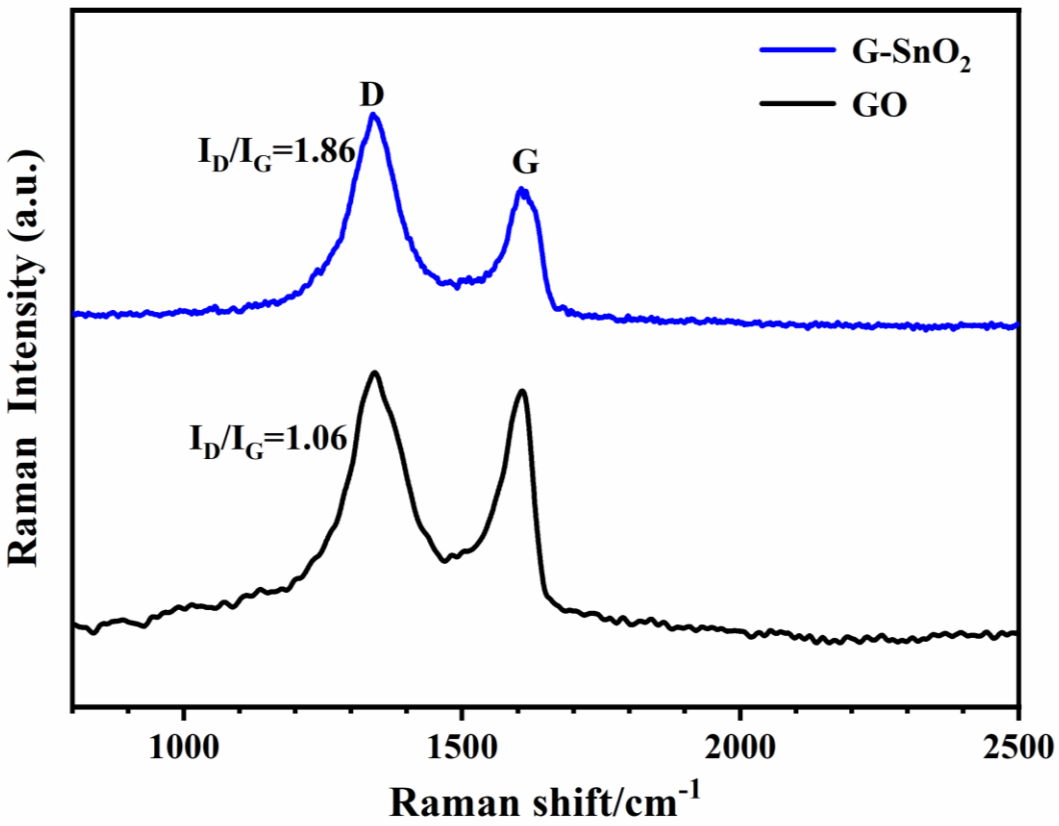

Figure 8. Raman spectra of GO and the SnO_2/G composite coatings prepared at 60 °C with a potential range from 0.6 to -1.1 V (vs. SCE).

To investigate the chemical composition, Fourier transform infrared spectroscopy (FT-IR) of the GO, SnO_2, and SnO_2/G composite coatings was performed, and the results are shown in Figure 9. The GO, SnO_2 and SnO_2/G composite coatings all have absorption peaks at 3430 cm^{-1}. The absorption peaks for the GO and SnO_2/G composite coatings originate from the -OH stretching vibrations of the sample. Furthermore, the absorption peak for SnO_2 here is entirely due to the water content. The absorption peaks at 1664 cm^{-1} and 1625 cm^{-1} can be attributed to the bending vibration of O-H. The absorption peak of GO at 1726 cm^{-1} can be attributed to C=O, and the absorption peak at 868 cm^{-1} can be attributed to O-C=O, which proves the presence of -COOH. The peaks at 1224 cm^{-1} and 1050 cm^{-1} can be attributed to C-O-C (epoxy group). The Sn-O stretching vibration occurs in the 800-300 cm^{-1} region. The Sn-O stretching vibration is usually at 670 cm^{-1} and 560 cm^{-1}. According to the nanoscale effect, the Sn-O stretching vibrational absorption peak for the SnO_2 sample appears at 620 cm^{-1}, and the O-Sn-O angular vibration absorption peak appears at 520 cm^{-1}. The infrared spectrum for SnO_2 in the SnO_2/G composite coating contains a single peak at 592 cm^{-1}. By comparing the FT-IR spectra of GO and the SnO_2/G composite coatings, it can be seen that although the -OH peak of the SnO_2/G composite coating decreases and the peaks for C=O, OC=O and C-O-C (epoxy) disappear, the vibrational peak of the graphene carbon skeleton at 1383 cm^{-1} is clearly stronger [34~36]. These observations show that the oxygen-containing functional groups on GO (-COOH, C-O-C, and -OH) were reduced during the electrodeposition of the SnO_2/G composite coatings, which corresponds well with the XPS test results.

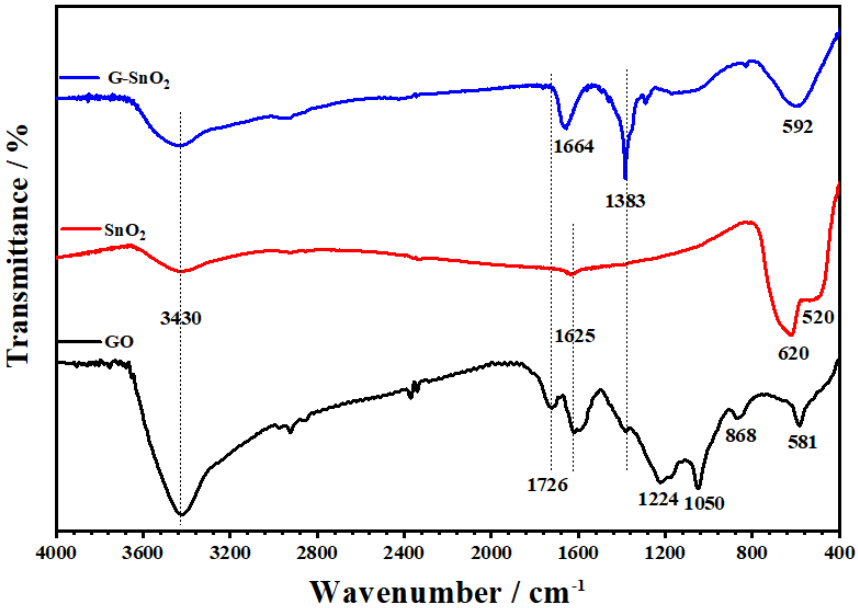

Figure 9. FT-IR spectra of GO, SnO_2 and the SnO_2/G composite coating prepared at 60 °C with a potential range from 0.6 to -1.1 V (vs. SCE).

3.3 Electrochemical test

The SnO_2/G composite coating is prepared by electrodeposition directly on the aluminum alloy electrode by cyclic voltammetry. Figure 10 shows the polarization curves of composite coatings prepared with different potential ranges in mixed acid solutions (0.5 M H_2SO_4 + 2 ppm HF). The corresponding electrochemical parameters are shown in Table 3. E_{corr} is the corrosion potential, β_a is the slope of the anode branch, and i is the corrosion current density. When the potential is in the range of 0.6~ -1.1 V, the corrosion potential is more positive, and the corrosion current density is smaller, so the corrosion resistance is greatest [12]. The protection efficiency (η) is generally calculated through the following relationship [37~39]:

$$\eta(\%) = \frac{i^0_{corr} - i_{corr}}{i^0_{corr}} \times 100 \quad (5)$$

where i^0_{corr} and i_{corr} are the corrosion current densities of the bare Al alloy and the coated Al alloy, respectively.

The protective efficiency of the deposited coating layer on the aluminum alloy substrate, as calculated by Equation (5), reaches 99.90%. The protective efficiency of the composite coating on the aluminum alloy substrate prepared in the range of 0.6~ -0.8 V (vs. SCE) and 0.6~ -1.5 V (vs. SCE) is slightly lower than that of the composite coating prepared in the potential range of 0.6~ -1.1 V (vs. SCE), indicating that a suitable potential range can be used to prepare a dense SnO_2/G composite coating on the surface of the substance. The potential range affects the corrosion resistance. At the very negative potential of -1.1 V (vs. SCE), H_2 is generated on the surface of the aluminum alloy (cathode), and many pores are formed in the composite coating, which reduces the anticorrosion properties of the deposit coating on the aluminum alloy substrate.

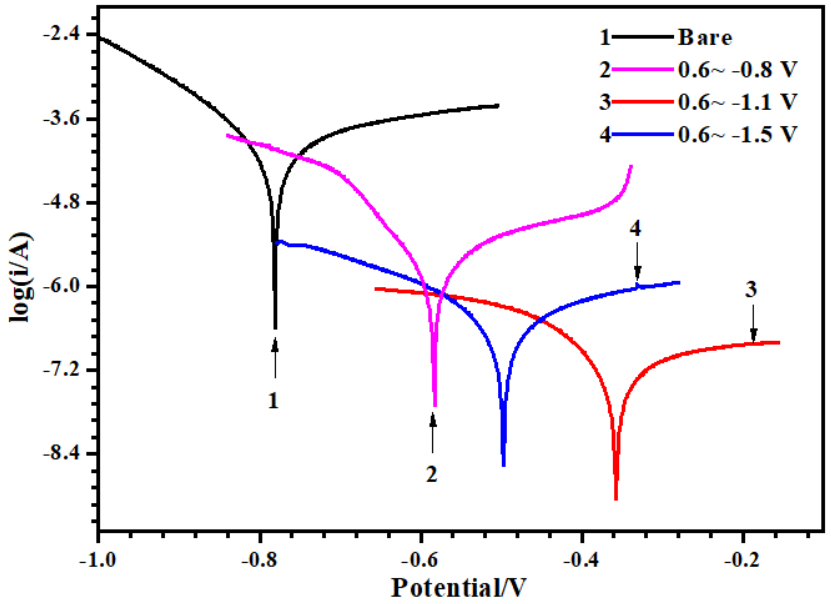

Figure 10. Polarization curves of SnO_2/G composite coatings prepared at different potential ranges under 60 °C in a mixed acid solution (0.5 M H_2SO_4 + 2 ppm HF).

Table 3. Electrochemical parameters of polarization curves of SnO_2/G composite coatings prepared at different potential ranges

Samples	E_{corr}, V	β_a, mV/dec	i_{corr}, A/cm^2	η, %
bare	-0.781	287	1.024×10^{-4}	/
0.6~-0.8 V	-0.583	241	2.040×10^{-6}	98.00
0.6~-1.1 V	-0.357	378	1.052×10^{-7}	99.90
0.6~-1.5 V	-0.497	253	3.633×10^{-7}	99.65

Furthermore, Figure 11 and Figure 12 show Nyquist plots and Bode plots, respectively, for the SnO_2/G composite coating prepared at different potential ranges in an acidic solution. Fig. 11 shows that the capacitance resistance loop of the SnO_2/G composite coating prepared by different potential ranges is much larger than that of the bare substance, which indicates that the composite coating layer on the surface of the substance increases the charge transfer resistance of the aluminum alloy surface [11]. The Nyquist plots of the composite coatings prepared at potentials ranging from 0.6 ~ -0.8 V (vs. SCE) are composed of loops at high frequencies, loops at intermediate frequencies, and a straight line at low frequencies, which are caused by charge transfer resistance, coating resistance and Weber resistance (Warburg), respectively. The dissolution and diffusion of the oxide coating on the substance usually causes Warburg resistance, indicating that the composite coating prepared in this potential range does not completely cover the surface of the substrate. The capacitive resistance loop shapes of the composite coatings prepared in the potential range of 0.6 ~ -1.1 V (vs. SCE) and 0.6 ~ -1.5 V (vs. SCE) are similar and much larger than those of bare aluminum alloys.

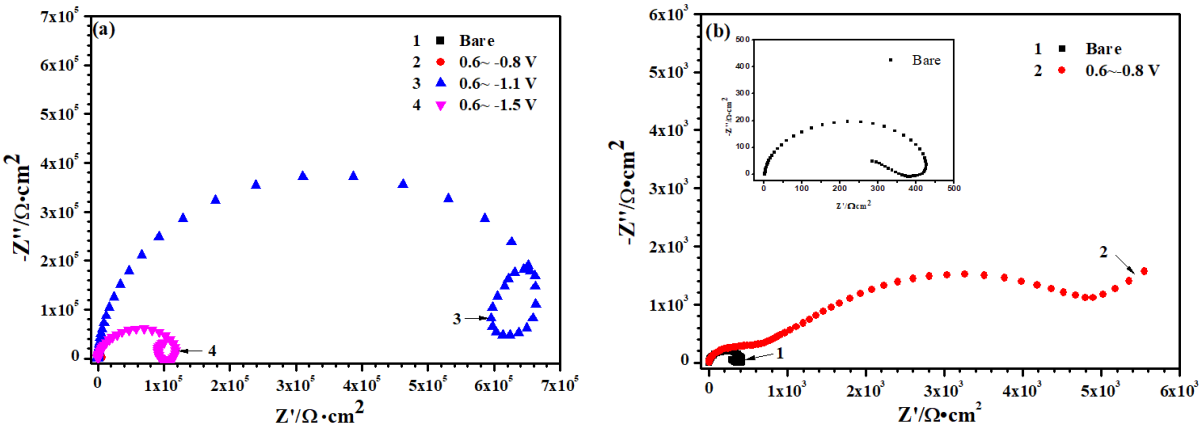

Figure 11. Nyquist diagram (a) and partially enlarged Nyquist diagram (b) of SnO_2/G composite coatings prepared at different potential ranges in an acidic solution (0.5 M H_2SO_4 + 2 ppm HF).

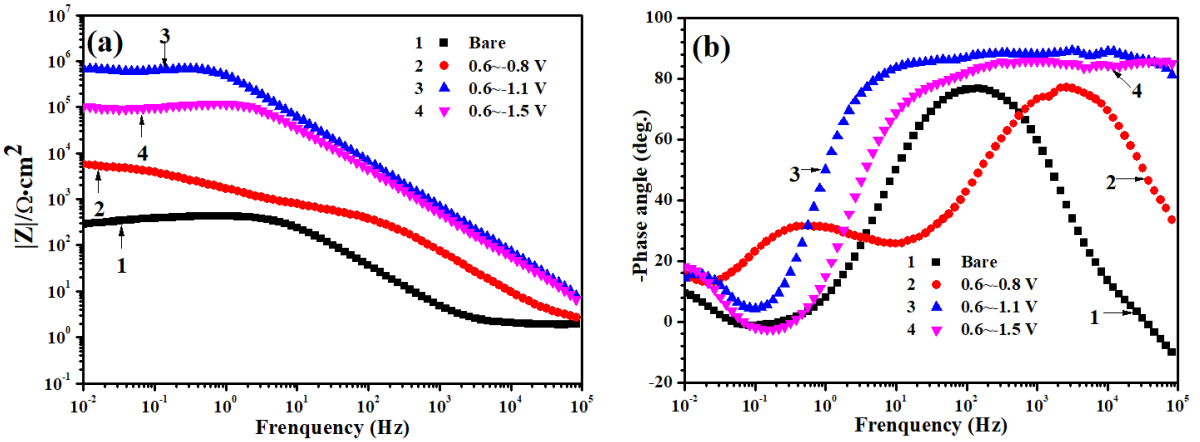

Figure 12. Bode impedance-frequency diagram (a) and Bode phase-frequency (b) diagram of SnO_2/G composite coatings prepared at different potential ranges in an acidic solution (0.5 M H_2SO_4 + 2 ppm HF)

Moreover, the capacitive arc of 0.6 to -1.1 V (vs. SCE) is the largest, which shows that the composite coating prepared by 0.6 to -1.1 V (vs. SCE) has the best protection effect on the aluminum alloy substrate. In general, the total impedance modulus | Z | represents the corrosion resistance of the sample at low frequencies in the test system. When the total impedance modulus is large, the anticorrosion properties of the sample are superior [40]. As shown in Fig. 12(a), the | Z | value for the range 0.6 to -1.1 V (vs. SCE) reaches 10^6 Ω·cm^2, which is greater than that reached for the other potential ranges and for bare aluminum alloy at 0.01 Hz. These results are consistent with the polarization curves.

To study the corrosion resistance and stability of the SnO_2/G composite coating for different immersion times in a strongly mixed acid solution, potentiostatic tests were carried out. From Fig. 13(a), it can be seen that the current density of the bare aluminum alloy decreases rapidly and exhibits large fluctuations. When the test time is close to 6 hours, the current density remains approximately stable at 2×10^{-4} A/cm^2. However, the current density of the SnO_2/G composite coating is essentially unchanged at 1×10^{-6} A/cm^2. The current density of the coating in the anode environment is 2

magnitudes lower than that of the bare aluminum alloy and remains stable over 6 hours of the test. This shows that the modified aluminum alloy containing the SnO_2/G composite coating has very good long-term operational stability under an anodic environment. Figure 13(b) shows the current density versus time for the bare aluminum alloy and the modified aluminum alloy with the SnO_2/G composite coating under a potential of -0.1 V (vs. SCE). As seen from the figure, the current density of the bare aluminum alloy as a cathode first rapidly increases and then remains at approximately 3×10^{-5} A/cm^2. While the current density of the SnO_2/G composite coating increases only slightly to no more than 1.2×10^{-6} A/cm^2, the SnO_2/G composite coating still plays a certain role in protecting the aluminum alloy substrate. Based on the above experimental results, it can be concluded that the modified aluminum alloy has good long-term operational stability in both anodic and cathodic environments.

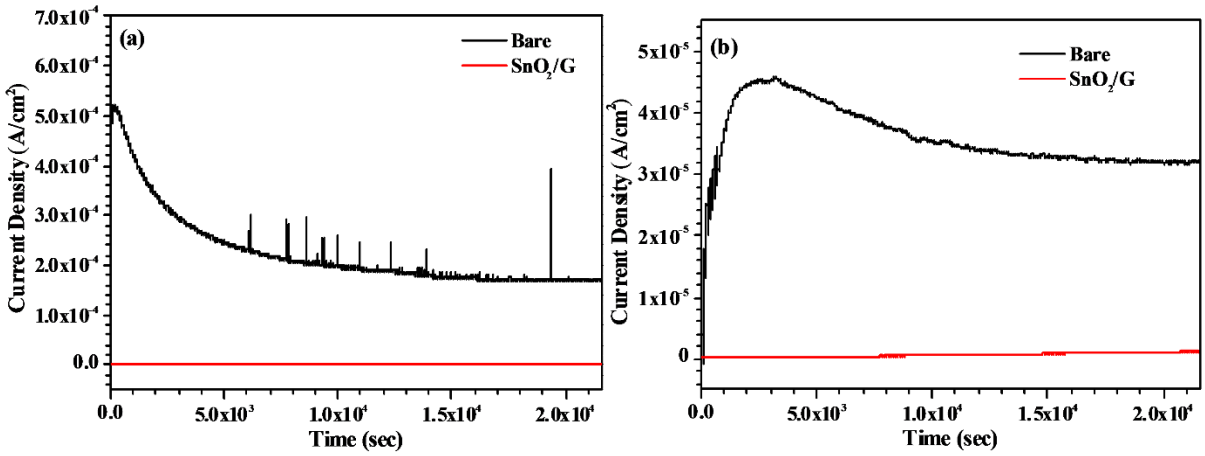

Figure 13. Potentiostatic polarization test: (a) potential at 0.6 V (vs. SCE); (b) potential at -0.1 V (vs. SCE).

Figure 14 shows the polarization curves of the SnO_2/G composite coating prepared in the potential range from 0.6 to -1.1 V (vs. SCE) after immersion in a mixed acid solution (0.5 M H_2SO_4 + 2 ppm HF) for different immersion times. The corresponding polarization curve parameters are listed in Table 4. According to Fig. 14 and Table 4, the protection efficiency of the SnO_2/G composite coating on the aluminum alloy substrate decreases as the immersion time increases. The corrosion potential of the SnO_2/G composite coating is -0.340 V in the simulation solution for the fuel cell without immersion (0 h). The corrosion potential is positively shifted 0.441 V relative to the bare aluminum alloy (-0.781 V), and the corresponding corrosion current density compared with the bare aluminum alloy (1.024×10^{-4}) is 1.243×10^{-8} A/cm^2. Via calculations, it can be seen that the corrosion current density decreases by 4 orders of magnitude, and the protection efficiency of the aluminum alloy substrate reaches 99.99%. The corrosion potential of the sample after immersion for 8 h is negatively shifted by 0.049 V relative to the corrosion potential of the sample without immersion, the corrosion potential changes to 3.565×10^{-8} A/cm^2, and the protection efficiency of the aluminum alloy substrate is maintained at a high value of 99.97%. This indicates that the composite coating still exhibits a very good protective effect on the aluminum alloy substrate after immersion in the acid solution for 8 h [11~12]. When the immersion time is extended to 24 h, the corrosion current density increases to 2.061×10^{-7} A/cm^2, and the protection efficiency decreases to 99.80%. When the immersion time is

increased to 72 h, the corrosion current density of the sample becomes 6.903×10^{-7} A/cm^2, and the protection efficiency drops to 99.33%. This shows that with increasing immersion time, the corrosion medium continuously destroys the SnO_2/G composite coating and diffuses through the pores to the aluminum alloy substrate. Although the corrosion current density of the sample immersed for 72 hours increases to 6.903×10^{-7} A/cm^2, the corrosion current density is still 3 orders of magnitude lower than that of the bare substance, showing that the SnO_2/G composite coating has better stability in an acid solution [11].

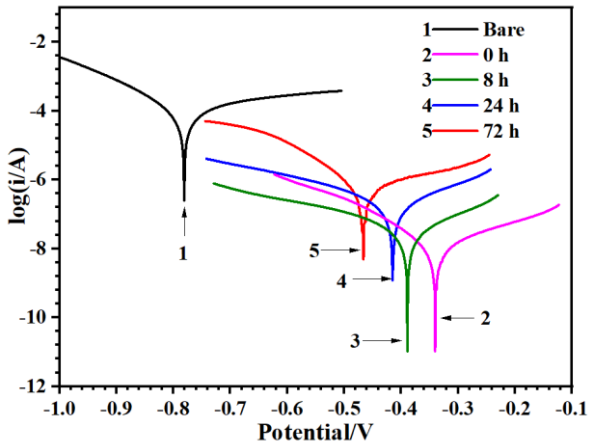

Figure 14. Polarization curves of the bare Al alloy and the SnO_2/G composite coating in an acidic solution (0.5 M H_2SO_4 + 2 ppm HF) for different immersion times.

Table 4. Electrochemical parameters of bare Al alloy and SnO_2/G composite coating in an acidic solution (0.5 M H_2SO_4 + 2 ppm HF) for different immersion times obtained from the polarization curves.

Samples	E_{corr}, V	β_a, mV/dec	i_{corr}, A/cm^2	η, %
bare	-0.781	287	1.024×10^{-4}	/
0 h	-0.340	182	1.243×10^{-8}	99.99
8 h	-0.389	150	3.565×10^{-8}	99.97
24 h	-0.415	163	2.061×10^{-7}	99.80
72 h	-0.466	278	6.903×10^{-7}	99.33

Figure 15 and Figure 16 show the Nyquist and Bode diagrams of the SnO_2/G composite coating prepared in the potential range from 0.6 to -1.1 V after immersion in an acid solution for different times. According to Fig. 15, the diameter of the Nyquist plot for the sample without immersion is the largest, and as the immersion time increases, the diameter of the capacitive reactance loop of the sample decreases continuously, indicating that the corrosion resistance of the SnO_2/G composite coating decreases as the immersion time increases [11]. As shown in Figure 16 (a), the total impedance |Z| of the sample at the lowest frequency decreases as the immersion time increases, which indicates

that when the immersion time is prolonged, the corrosion resistance of the SnO_2/G composite coating decreases [40].

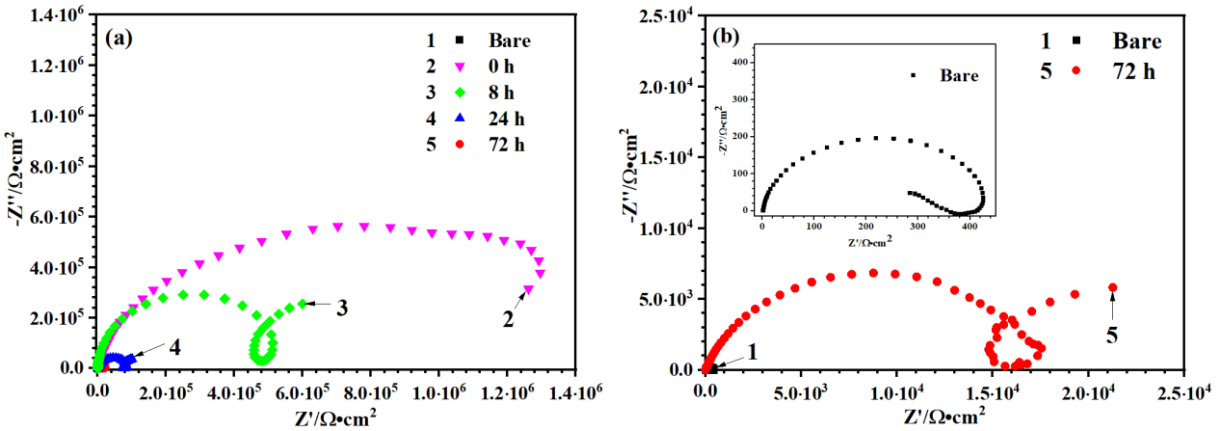

Figure 15. Nyquist diagram (a) and partially enlarged Nyquist diagram (b) of the SnO_2/G composite coating in an acid solution (0.5 M H_2SO_4 + 2 ppm HF) for different immersion times.

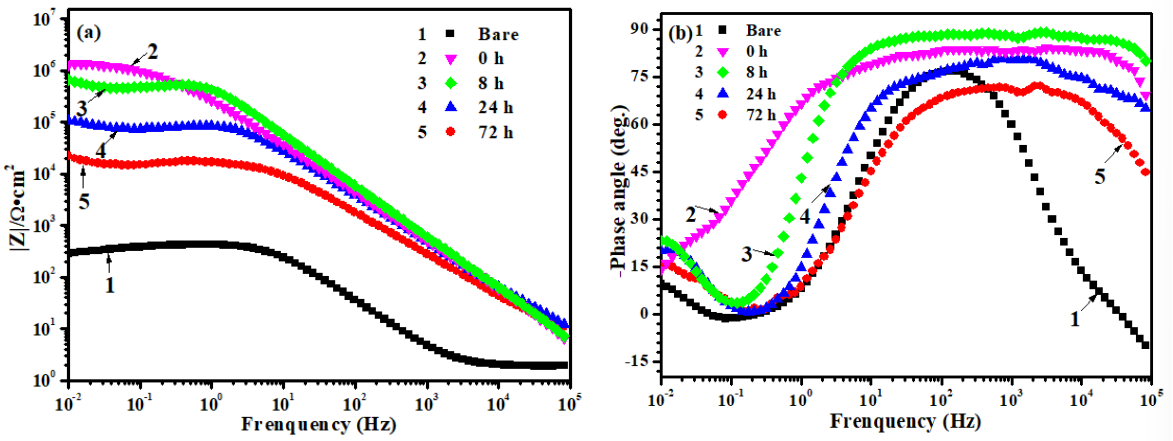

Figure 16. Bode impedance-frequency diagram (a) and Bode phase-frequency diagram (b) of the SnO_2/G composite coating in a mixed acid solution (0.5 M H_2SO_4 + 2 ppm HF) for different immersion times.

Anticorrosive coatings are a common strategy for corrosion protection of metals. Thus, a comparison of various carbon-based coatings for corrosion protection and corrosion inhibition efficiency is summarized in Table 5. The substrate used is steel or an Al alloy. The test solution is an acidic solution or a NaCl solution. Graphene/organic coatings [41~43], functionalized graphene oxide coatings [44~46], carbon coatings [47] and graphene/nanoparticle coatings [11] were investigated for corrosion protection of metals.

Graphene coatings with structural defects cannot provide stable corrosion resistance to metals. Chemical modification of graphene requires other chemical additives **[**44~46**]**. A complex preparation process is usually required for graphene composite coatings **[**11, 41~43**]**. Challenges remain in

dispersion and structure control for effective corrosion protection. The pyrolysis process occurs at high temperatures [47].

In this work, the electrodeposition process is a facile and highly effective strategy. Compared with other studies, a time-saving approach for obtaining anticorrosive coatings on Al alloys in acidic environments is proposed in this paper. Furthermore, this process avoids complex chemical modification, structure control and dispersion. Based on the barrier ability of graphene and the stability of SnO_2, a highly effective coating is designed. As expected, the electrodeposited SnO_2/graphene composite coating exhibits a high inhibition efficiency (99.97%) in an acidic solution, which is higher than those of the coatings listed in Table 5. It is a promising candidate for corrosion protection on Al alloys in acidic environments.

Table 5. Comparison of anticorrosive carbon-based coatings reported in previous works.

Coating	Substrate	Environment	Immersion time (h)	*η*, %	Ref
Sulfonated oligoanilines /GO (Coating)	Q325 steel	3.5wt% NaCl solution	/	96.42	[41]
Urtica Dioica leaves extract /Polyaniline nanofibers/GO	Mild steel	3.5wt% NaCl solution	48	77.39	[42]
Epoxy/SiO_2-GO nanohybrid (Coating)	Mild steel	3.5wt% NaCl solution	/	99.30	[43]
Diaminopyridine/GO	Mild steel	1 M HCl	3	96.73	[44]
p-Aminophenol-GO	Mild steel	1 M HCl	/	92.86	[45]
Aminoazobenzene/GO	Mild steel	1 M HCl	/	94.65	[46]
Nitrogen doped carbon coating	6061Al alloy	0.5 M H_2SO_4 + 2 ppm HF	4	99.91	[47]
SnO_2/G composite coating	6061Al alloy	0.5 M H_2SO_4 + 2 ppm HF	5	99.70	[11]
SnO_2/G composite coating	5052 Al alloy	0.5 M H_2SO_4 + 2 ppm HF	8 24 72	99.97 99.80 99.33	This work

4. CONCLUSIONS

A SnO_2/G composite coating was electrodeposited on an aluminum alloy by cyclic voltammetry at an optimal potential range of 0.6~-1.1 V (vs. SCE) with a scanning rate of 25 mV/s and a GO concentration of 0.06 mg/ml. The corrosion current density of the SnO_2/G composite coating prepared under the optimal conditions was 1.243×10^{-8} A/cm^2 in an acid solution (0.5 M H_2SO_4 + 2 ppm HF), which was four orders of magnitude lower than that of the bare aluminum alloy (1.024×10^{-4} A/cm^2). The protective efficiency of the composite coating was above 99%, confirming that the coating exhibited good corrosion resistance in such a test system. Additionally, the composite coating prepared in the potential range from 0.6~ -1.1 V (vs. SCE) exhibited good stability according to the

polarization potential test. Furthermore, the protective efficiency of the composite coating was 99.33% after immersion for 72 h, indicating that the coating exhibited long-term stability in an acidic environment. This electrodeposited SnO_2/graphene composite coating shows good potential for corrosion protection on aluminum alloys in acidic environments.

ACKNOWLEDGMENTS
This work was financially supported by funding from the National Natural Science Foundation of China (NSFC 51972207), Science and Technology Commission of Shanghai Municipality (No. 19DZ2271100), and Science and Technology Commission of Shanghai Municipality (No. 21ZR1425100)

References

1. T. L. P. Galvão, I. Sousa, M. Wilhelm, J. Carneiro, J. Opršal, H. Kukačková, V. Špaček, F. Maia, J. R. B. Gomes, J. Tedim, M. G. S. Ferreira, *Chem. Eng. J.*, 341(2018) 526-538.
2. Y. Liu, W. Yao, G. Wang, Y. Wang, A. S. Moita, Z. Han, L. Q. Ren, *Chem. Eng. J.*, 303(2016) 565-574.
3. A. G. González-Gutiérrez, M. A. Pech-Canul, G. Chan-Rosado, P. J. Sebastian, *Fuel,* 235 (2019) 1361-1367.
4. F. Zhang, P. F. Ju, M. Q. Pan, D. W. Zhang, Y. Huang, G. L. Li, X. G. Li, Self-healing mechanisms in smart protective coatings: A review, *Corros. Sci*., 144 (2018) 74-88.
5. Y. Lu, J. Y. Hu, S. Li, W.S.Tang, *Electrochim. Acta*, 278(2018) 124-136.
6. E. Fortunato, P. Barquinha, R. *Adv. Mater.*, 24(2012) 2945-2986.
7. D. H. Wei, S. Y. Zhong, H. Zhang, X. J. Zhang, C. Zhu, J. F. Duan, L. J. Li, Z. Y. Chen, P. Liu, G. H. Zhang, H. G. Duan, *Electrochim. Acta*, 290(2018) 312-321.
8. Y. Wang, C. H. Duan, J. S. Li, W. Han, M. Zhao, L. L. Yao, Y. Y. Wang, C. Yan, T. G. Jiu, *ACS Appl. Mater. Interfaces*, 10(2018) 20128-20135.
9. Q. Wali, A. Fakharuddin, R. Jose, *J. Power Sources*, 293(2015) 1039-1052.
10. R. Zhou, Y. Han, J.Y. Cao, M. Li, G.R. Jin, Y.Z. Du, H. T. Luo, Y.C. Yang, L.Z. Zhang, B. Su, *ACS Appl. Mater. Interfaces*, 10(2018) 30191-30200.
11. L. H. Yang, Y. X. Wan, Z. L. Qin, Q. J. Xu, Y. L. Min, *Corros. Sci*., 130 (2018), 85-94.
12. H. Cao, Z. Tan, G. Fan, Q. Guo, Y. Su, Z. Li, D.-B. Xiong, *Compos. Part B: Eng.*, 191(2020) 107965.
13. X. Yao, Y. L. Zhao, *Chem*, 2(2017) 171-200.
14. Z. S. Wu, A. Winter, L. Chen, Y. Sun, A. Turchanin, X. L. Feng, K. Müllen, *Adv. Mater.*,24 (2012) 5130-5135.
15. S. I. Wong, J. Sunarso, B. T. Wong, H. Lin. A. M. Yu, B. H. Jia, *J. Power Sources*, 396(2018)182-206.
16. G. D. Kwon, E. Moyen, Y. J. Lee, J. Joe, D. Priba, *ACS Appl. Mater. Interfaces*, 10(2018) 29486-29495.
17. H. J. Yang, L. Geng, Y. T. Zhang, G. Chang, Z. L. Zhang, X. Liu, M. Lei, Y. B. He, *Appl. Surf. Sci*., 466(2019) 385-392.
18. A. Subramanian, Z.H. Pan, G. L. Rong, H. F. Li, L. S. Zhou, W. F. Li, Y. C. Qiu, Y. J. Xu, Y. Hou, Z. Z. Zheng, Y. G. Zhang, *J. Power Sources*, 343(2017) 39-46.
19. R. Ding. W. H. Li, X. Wang, T. J. Gui, B. J.Li, P. Han, H. W. Tian, A. Liu, X. Wang, X. J. Liu, X. Gao, W. Wang, L. Y. Song, *J. Alloys Compd.*, 764(2018) 1039-1055.
20. M. H. Wang, Q. H. Li, X. G. Li, Y. C. Liu, L. Z. Fan, *Appl. Surf. Sci*., 448(2018)351-361.

21. J. C. Lei, Y. W. Hu, Z. S. Liu, G. J. Cheng, K. J. Zhao, *ACS Appl. Mater. Interfaces*, 9(2017) 11902-11908.
22. S. Naghdi, I. Jevremović, V. Mišković-Stanković, K. Y. Rhee, *Corros. Sci*., 113(2016) 116-125.
23. B. Y. Jin, D. B. Xiong, Z. Q. Tan, G. L. Fan, Q. Guo, Y. S. Su, Z. Q. Li, D. Zhang*, Carbon,* 142 (2019) 482-490.
24. J. B. Zhang, R. W. Shu, Y. P. Ma, X. Y. Tang, G. Y. Zhang, *J. Alloys Compd.*,777(2019) 1115-1123.
25. K. Ghosh, C. Y. Yue, *Electrochim. Acta*, 276(2018) 47-63.
26. C.P. Lee, K. Y. Lai, C.A. Lin, C.T. Li, K.C. Ho, C.I, Wu, S.P. Lau, J.H. He, *Nano Energy*, 36(2017) 260-267.
27. D. N. Wang, X. F. Li, J. J. Wang, J. L. Yang, D. S. Geng, R. Y. Li, M. Cai, T.-K. Sham, X. L. Sun, *J. Phys. Chem.C.*, 116(2012) 22149-22156.
28. Q. H. Tian, Z. M. Hong, J. Z. Chen, L. Yang, *Chem. Eng. J.*,342(2018)266-273.
29. F. Zoller, K. Peters, P. M. Zehetmaier, P. Zeller, M. Döblinger, T. Bein, Z. Sofer, D.Fattakhova-Rohlfing, *Adv. Funct. Mater.*, 28(23)1706529.
30. J. L. Yu, H. Y. Liu, S. Q. Song, Y. Wang, P. Tsiakaras, *Appl. Catal. A Gen.*, 545(2017)159-166.
31. H. Cao, Z. Tan, M.H. Lu, G. Ji, X.J. Yan, C. Di, M.Y. Yuan, Q. Guo, Y.S. Su, A. Addad, Z. Li, D.B. Xiong, *Carbon,* 150(2019) 60-68.
32. H. Cao, D.B. Xiong, Z. Tan, G. Fan, Z. Li, Q. Guo, Y. Su, C. Guo, D. Zhang, *J. Alloy. Compd.*, 771(2019)228-237.
33. B. H. Zhang, Z. H. Guo, Z. Zuo, W. Pan, J. T. Zhang, *Appl. Catal. B Environ.*, 239(2018)441-449.
34. K. C. Lam, B. Huang, S. Q. Shi, *J. Mater. Chem. A.*, 5(2017) 11131-11142.
35. Y. C. Dun, X. H. Zhao, Y. M. Tang, S. Dino, Y. Zuo, *Appl. Surf. Sci.*, 437(2018)152-160.
36. J. F. Liang, W. Wei, D. Zhong, Q. L. Yang, L. D. Li, L. Guo, *ACS. Appl. Mater. Interfaces*, 4(2012)454-459.
37. H. Cao, M. Fang, W. Jia, X. Liu, Q. Xu, *Compos. Part B: Eng.*, 228 (2022) 109427.
38. G. Sığırcık, T. Tüken, M. Erbil, *Corros. Sci*., 102 (2016) 437-445.
39. Q. B. Zhang, Y. X. Hua, *Electrochim. Acta*, 54(2009) 1881-1887.
40. H. Cao, *Colloids Surf. A: Physicochem. Eng. Asp.,* 652 (2022) 129893.
41. H. Lu, S. T. Zhang, W. H. Li, Y. A. Cui, T. Yang, *ACS Appl. Mater. Interfaces*, 9(4) (2017) 4034-4043.
42. B. Ramezanzadeh, P. Kardar, G. Bahlakeh, Y. Hayatghei, M. Mahdavian, *J. Phys. Chem. C*, 121 (37) (2017) 20433-20450.
43. S. Pourhashem, M. R. Vaezi , A. Rashidi, *Surf. Coat. Technol.*, 311 (2017) 282-294.
44. R. K. Gupta, M. Malviya, C. Verma, N.K. Guptaa，M. A. Quraishi, *RSC Adv.*, 7 (62) (2017) 39063-39074.
45. R.K. Gupta, M. Malviya, K.R. Ansari, H. Lgaz, D.S. Chauhan, M.A. Quraishi, *Mater. Chem. Phys.*, 236 (2019) 121727.
46. R. K. Gupta, M. Malviya, C. Verma，M. A. Quraishi, *Mater. Chem. Phys.*, 198 (2017) 369-373.
47. Y. W. Zeng, H. J. Cao, W. H. Jia, Y. L. Min, Q. J. Xu, *Surf. Coat. Tech.*, 445(2022)128709.